inventions

MDPI

Article

Investigation of $BaFe_{12}O_{19}$ Hexaferrites Manufactured by Various Synthesis Methods Using a Developed Pulsed Magnetometer

Dmitry V. Wagner [1,2,*], Katerina V. Kareva [1,2], Viktor A. Zhuravlev [1,*], Olga A. Dotsenko [1] and Roman V. Minin [3]

[1] Faculty of Radiophysics, National Research Tomsk State University, Lenina Ave., 36, 634050 Tomsk, Russia
[2] Scientific Laboratory for Terahertz Research, National Research Tomsk State University, Lenina Ave., 36, 634050 Tomsk, Russia
[3] Tomsk Scientific Center, Siberian Branch of the Russian Academy of Sciences, Akademichesky Ave., 10/4, 634055 Tomsk, Russia
* Correspondence: wagner_dv@yahoo.com or wagner_dv@mail.tsu.ru (D.V.W.); ptica@mail.tsu.ru (V.A.Z.)

Abstract: The manufacture and study of the properties of magnetic materials requires the development of new automated devices for measuring their magnetic properties. To obtain nanosized materials with a pure phase, it is necessary to modernize former methods and develop new methods for synthesizing materials. As part of this study, a pulse magnetometer was made to study magnetic hysteresis loops. An exceptional feature of this device is the ability to conduct studies of the full cycle of the hysteresis loop using pulsed magnetic fields. M-type $BaFe_{12}O_{19}$ hexagonal ferrites were synthesized by standard ceramic, mechanochemical, and sol–gel methods. The structural, phase, and magnetic characteristics of the barium hexaferrites were studied. Methods for the synthesis of $BaFe_{12}O_{19}$ hexagonal ferrites were estimated and compared. Their structural and magnetic properties essentially depend on the method of synthesis. The mechanochemical technology makes it possible to obtain materials without impurity phases through the use of hydrated reagents in the synthesis. The use of sol–gel technology allows the synthesis to be carried out at much lower temperatures.

Keywords: hexaferrite; pulse magnetometer; magnetization; coercive force; sol–gel technology; mechanochemical synthesis

Citation: Wagner, D.V.; Kareva, K.V.; Zhuravlev, V.A.; Dotsenko, O.A.; Minin, R.V. Investigation of $BaFe_{12}O_{19}$ Hexaferrites Manufactured by Various Synthesis Methods Using a Developed Pulsed Magnetometer. *Inventions* **2023**, *8*, 26. https://doi.org/10.3390/inventions8010026

Academic Editor: Alessandro Chiolerio

Received: 27 December 2022
Revised: 13 January 2023
Accepted: 14 January 2023
Published: 18 January 2023

1. Introduction

Ferrimagnetic materials have been of great interest over the years [1–4] for a variety of reasons. The first reason is the uniqueness of their properties. Hexagonal ferrites of all types (i.e., M, Y, W, Z, X, U) are simultaneously ferromagnets and dielectrics, have low electrical conductivity, and have high quantities of magnetic properties, such as saturation magnetization and magnetic permeability. Therefore, ferrite materials are used in many branches of technology and science, including electrical engineering and automation (e.g., permanent magnets, transformers, electromagnetic relays, ferrite filters, measuring instruments) [4,5], radio engineering (e.g., antennas, phase shifters, attenuators, circulators, absorbers of electromagnetic radiation) [6–10], computer technologies (e.g., elements of magnetic memory) [11], medicine (e.g., transportation of drugs, local hyperthermia, tissue engineering) [12–15], and in lithium-ion batteries [16].

The second reason is the variety of methods for synthesizing ferrites, making it possible to manufacture ferrites with improved magnetic properties, such as higher quantities of coercive force and shift in the resonance frequency of domain wall resonance. The most common and well-established method is the standard ceramic technology. This is used, as a rule, to obtain monolithic samples consisting of micro-sized grains. The technology includes the following steps: mixing the initial components into a homogeneous mixture,

grinding the mixture in a wet state using laboratory mills, drying and pressing the crushed powder, and calcination at the required temperatures to carry out a chemical reaction between the components. These stages are usually carried out several times to obtain single-phase materials [1].

Another common synthesis method for producing micro-sized ferrite powders is self-propagating high-temperature synthesis (SHS). To date, it has been studied and proven that the possibility of autowave processes such as combustion in SHS is due to the release of heat during the chemical interaction of the components of the initial mixture and its transfer from hot layers of matter to cold ones. The principal feature of the SHS method is the propagation along the reaction system of the processes of destruction of old and restoration of new chemical bonds. As a result of a chemical reaction, electrons are exchanged between the atoms of the starting substances. The formation of an electromotive force (EMF) during a reaction includes the formation of charged particles on the interface between individual granules of the initial components and is determined by the state of the reaction medium (e.g., chemical and phase composition, temperature). The main stages of the SHS process are the preparation of the initial raw material, synthesis in the self-propagation mode, and the stage of cooling the obtained product, which results in the formation of the final crystalline structure of the finished products [17,18].

Chemical methods of synthesis are also actively used—for instance, the sol–gel method, the chemical co-precipitation method, the mechanochemical method, and their other variations [4,7,10,12–15,19]. The chemical methods of synthesis from salt systems are carried out by operations that include co-precipitation and precipitation, which are products of the chemical interaction of solutions of salts or their bases. The initial reagents can include nitric acid and hydrochloric acid, as well as water-soluble salts of metals ($BaCl_2$, $FeCl_3$, $CuSO_4$). Precipitated materials are introduced into their solutions: $(NH_4)_2CO_3$—ammonium carbonate (carbonate); $(NH_4)_2C_2H_4$—ammonium oxalate (oxalate); NaOH—sodium hydroxide (hydroxide). The initial solutions of salts and precipitating substances are dissolved in distilled water, filtered from impurities, and then continuously stirred in the desired ratio. The precipitates are filtered and then washed with water to remove soluble impurities. After drying, grinding, and calcination (T = 300–800 °C), the salts decompose and turn into oxides [20]. The co-precipitation method is implemented in various versions: co-precipitation of all initial substances; separate precipitation of each substance and their subsequent mixing; or precipitation of one or more components, followed by mixing with oxides [20]. An effective method for the preparation of precursors is the mechanochemical method, which is based on an intense mechanical action on a mixture of reagents in planetary mills, attritors, and disintegrators.

Materials with a high degree of purity can be obtained via sol–gel technology. This method is carried out in several consecutive steps. First, the initial components are mixed and the formation of a sol is achieved—a colloidal solution in which liquid droplets, gas bubbles, or small solid particles of 1–100 nm in size are distributed in a liquid or gaseous dispersion medium. Next, the resulting suspension is converted into a gel by increasing the volume concentration of the dispersed phase or by changing the external conditions. Several consecutive processes, or just one of them (e.g., hydrolysis, condensation, ultrafiltration, drying, and heat treatment), create contacts between particles, which leads to the formation of a monolithic polymer gel, in which the molecules form a three-dimensional ordered network. In the last stage, ferrite powder is obtained by rapid heating to a temperature of 600 to 1200 °C. The particle sizes, depending on the selected components and the conditions of the synthesis being implemented, are in the range from several tens to hundreds of nanometers. The advantages of the sol–gel method include the high homogeneity of the resulting material—single-phase crystal structure—the ability to control the particle size, and the stoichiometric composition. Due to features of the method, the energy consumption is reduced. However, the most significant advantage of the sol–gel method is the mechanical properties of sols and gels, so it can be used to obtain fibers, needles, films, and composites that can be deposited on the surface [21]. The development, application and improvement

of these methods enable the synthesis of ferrite nanoparticles. As a result, opportunities for the research of nanomagnetism are arising, and new devices are being designed for application in the fields of spintronics and medical applications [13,14,22–26].

Based on the above, the study of the magnetic properties of ferrites is a priority task in the development of new materials and the theory of the physics of magnetic phenomena. Hysteresis loops of magnetic materials are most often studied. Analysis of loops allows the determination of the saturation magnetization, remanent magnetization, and coercive force of the materials under study. Moreover, from the shape of the loop, one can determine whether the material is magnetically hard or magnetically soft for attributing it to some area of practical application [27].

To study the magnetic properties of hard magnetic materials, it is necessary to generate high magnetic fields (HMFs) of at least 100 kOe, and this is a complex technical problem. Obtaining HMFs is possible with the use of impulse methods, which have been actively used and developed from the first half of the 20th century to the present [28]. The most common way to obtain a pulsed magnetic field is using an inductor connected to a charged bank of capacitors. Impulse installations of this kind, in addition to achieving HMFs, must include an impulse magnet that can withstand high mechanical stresses caused by ponderomotive forces. The magnitude of ponderomotive forces is directly proportional to the square of the magnetic field strength. Modern impulse magnets are not simple coils consisting of a wound conductive bar, but complex systems consisting of many functional components. The development of other parts of the impulse installations, such as the capacitor bank with auxiliary equipment, is not a difficult task, since these components are available on the commercial market and are mass-produced. There is no mass manufacturing of impulse magnets, because each such magnet is made for a specific task. Thus, the most important task in the development of any impulse installation is the development of an impulse magnet. Poor-quality manufacturing of a pulsed magnet will lead to its destruction at high magnetic field strengths due to deformation under the influence of mechanical stresses arising in the coils [29].

The most popular are pulse magnets whose coils are made of high-quality steel [29], heavy-duty conductive materials based on CuAg [30], and copper/stainless steel (Cu/SS) macrocomposite conductors [31]. Coils made from these materials can generate fields of up to 600 kOe. HMFs can also be produced using Bitter-type magnets [32], and the magnitude of these magnetic fields reaches 350 kOe, which is sufficient for studying the magnetic properties of hard magnetic materials. Magnets of this type are assembled from round disks with a radial slot, superimposed on one another along the axis of the magnet. Conductor disks alternate with dielectric disks, turning from layer to layer at a certain angle; thus, a conductive spiral is obtained. The main disadvantage of these magnets is the inhomogeneity of the magnetic field, which makes them unsuitable for the development of pulse installations for studying the magnetic properties of materials.

To obtain HMFs of up to 100 kOe, it is possible to use pulsed magnets made of copper. However, it is necessary to use structures to strengthen them in order to avoid their destruction during repeated use.

The objectives of this article were the development of a pulsed magnetometer and a study of the composition, structure, and magnetic properties of $BaFe_{12}O_{19}$ powder ferrimagnets synthesized by various methods using the developed pulse magnetometer.

2. Materials and Methods

2.1. Synthesis of Ferrite Samples

The $BaFe_{12}O_{19}$ hexaferrites studied in this work were fabricated by the ceramic (solid-phase) method, the mechanochemical method, and the sol–gel method.

Sample N1 was synthesized using solid-phase technology. To obtain the test sample, the metal oxides BaO (>99.9%) and Fe_2O_3 (>99.9%) were taken as the initial components, which were mixed in the following stoichiometric composition for the final product:

$$BaO + 6\ (Fe_2O_3) = BaFe_{12}O_{19}. \quad (1)$$

Before mixing, the powders were dehydrated in a drying chamber at (200 ± 10) °C for 3 h. The components were weighed on an HL-100 electronic balance («A&D», Toshima City, Japan) with an accuracy of ±0.01 g and then compacted in a hydraulic press at a pressure of 100 MPa. Preliminary calcination was carried out in an oxygen atmosphere at 1150 °C for 6 h. The shrinkage of the original samples was 15–20%, which corresponds to the standard ceramic technology. Then, the primary workpieces were broken in a mortar and re-ground in a vibrating mill for 35 ± 5 min together with iron balls. The resulting powder was repeatedly pressed in a hydraulic press at a pressure of 100 MPa and sintered to obtain the M-type phase in an oxygen atmosphere for 6 h at 1200 °C. From the resulting samples, a powder of the required size was obtained by grinding in a mortar and sifting through a system of analytical sieves to acquire a fraction with a grain size of less than 50 μm.

Sample N2 was prepared by the mechanochemical method. The following reaction was used to manufacture the $BaFe_{12}O_{19}$ powder:

$$BaCl_2 \cdot 2H_2O + 12FeCl_3 \cdot 6H_2O + 38NaOH = BaFe_{12}O_{19} + 38NaCl + 93H_2O \quad (2)$$

The reagents (>99%, all) were used as raw materials for the synthesis; iron and barium chlorides were used both in the form of crystalline hydrates and in the form of anhydrous salts. Hydrated barium chloride was taken in excess of 20% wt. To prevent local combustion and agglomeration of the reaction mixture during mechanical activation, sodium chloride was introduced as an inert additive, in an excess ratio relative to the reaction mixture, equal to 1:4. The mixture was sealed in hardened steel drums with steel balls of 5 mm in diameter. The synthesis of barium hexaferrite was carried out in an AGO-3 high-stress planetary mill (Russia, Novosibirsk) at a 1:10 ratio of the mass of the reaction mixture to the mass of the balls, for 60 min. The carrier and drum speeds were 640 revolutions per minute (rpm) and 1560 rpm, respectively. The resulting product was subjected to heat treatment at 200 °C for 2 h in air, after which it was washed by centrifugation (ROTANTA 430 R, «Hettich», Westphalia, Germany) with distilled water until the salts were completely removed. After heat treatment, the product was dried at 25 °C, and a hexaferrite structure was formed by calcining the powder in a muffle furnace in air at 1100 °C. A more detailed description of the synthesis is provided in [33].

To obtain sample N3, the sol–gel combustion method was used as described in [34]. This method is based on the creation of an initial colloidal nanosystem capable of reacting in the combustion mode. Aqueous solutions of barium nitrate $Ba(NO_3)_2$ (98%) and iron nitrate 9-aqueous $Fe(NO_3)_3\ 9H_2O$ (98%) were used as reagents. Citric acid ($C_6H_8O_7$) with a concentration of 1 M was used as an organic fuel. These reagents were mixed according to the following ratios:

$$[Ba(NO_3)_2]:[Fe(NO_3)_3 \cdot 9H_2O]:C_6H_8O_7 = [1]:[11.5]:25. \quad (3)$$

The choice of this ratio was based on previous studies [35], which reported that an excess of barium is necessary to ensure the formation of single-phase $BaFe_{12}O_{19}$ due to the fact that a small amount of barium volatilizes during combustion and calcination, which leads to a violation of stoichiometry [36].

Nitrates and citric acid were dissolved in water separately, after which the aqueous solutions were mixed. A concentrated solution of ammonium hydroxide (NH_4OH; >98%) was added dropwise to the prepared mixture with constant continuous stirring. This procedure continued until the pH of the solution reached 7. The pH of the medium

was measured with a Checker HI98103 portable digital pH meter (HANNA Instruments, Woonsocket, RI, USA). The resulting sol was heated on an ES-6120 magnetic stirrer (EKROS, Moscow, Russia) at a temperature of 80–90 °C for 5 h. After heating, the sol turned into a viscous gel, which foamed. Further heating of the resulting gel foam to 150–160 °C caused ignition and burning, which lasted for several minutes. The combustion product was a loose powder, which was ground in a mortar, turning into a fine powder. To remove organic impurities, the powder was calcined at 450 °C for 24 h. Finally, for the total formation of $BaFe_{12}O_{19}$ nanoparticles, the powder was annealed at 850 °C for 6 h. The synthesis of barium hexaferrite powders was carried out by the following chemical reaction:

$$Ba(NO_3)_2 + 12Fe(NO_3)_3 \cdot 9H_2O + C_6H_8O_7 = BaFe_{12}O_{19} + 38NO_2 + 6CO_2 + 112\ H_2O + 5O_2. \quad (4)$$

2.2. Development of the Pulse Magnetometer

To measure the main magnetic characteristics, we used the standard technique for measuring magnetization in a pulsed magnetic field, as described in sufficient detail in the monograph by D.B. Montgomery [37]. To study the behavior of magnetic hysteresis loops, a pulsed magnetometer was developed and manufactured (Figure 1). It contained an electric current pulse generation unit, a pulse solenoid, a system of measuring coils, a signal conversion and amplification unit, an L-154 analog-to-digital (AD) converter (L-Card, Moscow, Russia) connected to a personal computer, and a key for switching the direction of the magnetic field in the solenoid. As a system of measuring coils, three coils made of copper wire were used, which were placed coaxially. The coils No. 1 and No. 3 were connected to coil No. 2 with the same flux linkage and spaced apart from one another at a distance sufficient to eliminate the phenomenon of mutual induction. The discharge of a capacitor bank was used as a source of a pulsed magnetizing field, making it possible to obtain a magnetic field up to 100 kOe.

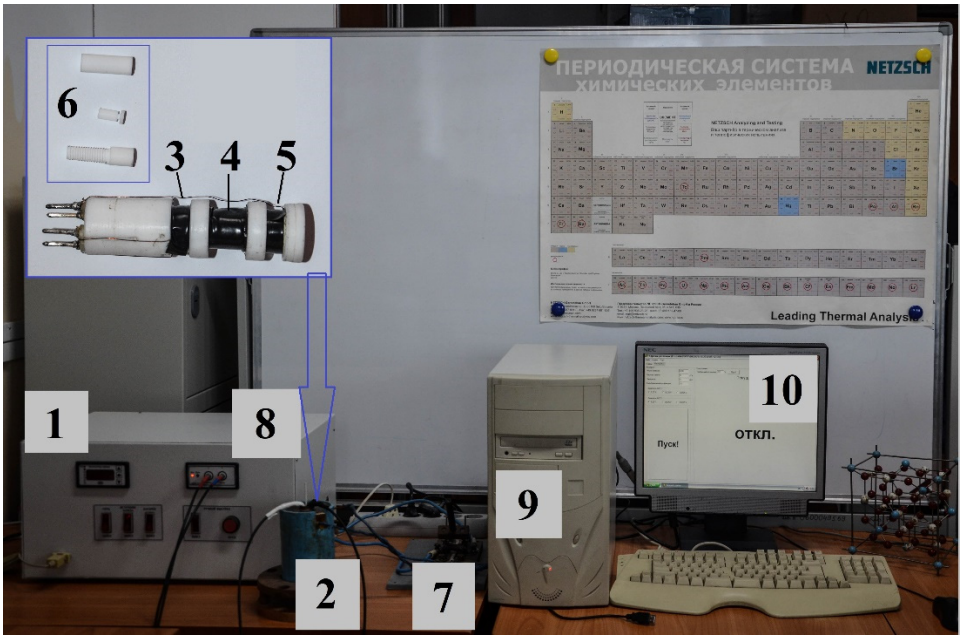

Figure 1. Pulse magnetometer: 1—electric current pulse generation unit; 2—impulse solenoid; 3, 5—compensation coils (No. 1 and No. 3, respectively); 4—measuring coil (No. 2); 6—powder sample container (disassembled); 7—key; 8—signal conversion and amplification unit; 9—personal computer; 10—working window of the program.

The electric current pulse formation unit (1) was connected to an alternating-current circuit with a voltage of 220 V and a frequency of 50 Hz. The unit contained 48 electrolytic capacitors (Yageo, New Taipei City, Taiwan) with a capacity of 470 microfarads each. Its

operating temperature range was from −40 to 105 °C. The pulse solenoid (pulse magnet) (2) was made by the staff of the Ferrite Physics Laboratory of TSU in 2012 and was a conventional coil wound with a three-core copper wire. A three-core copper wire was used to reduce the active resistance of the coil. The diameter of each core was 1.5 mm. The coil was filled with ED-20 epoxy glue (OOO NPK Astat, Dzerzhinsk, Russia). The winding was reinforced on the outside with a plastic pipe with a wall thickness of 6 mm. The inner diameter of the solenoid was 20 mm. The mechanical key (7) was needed to change the direction of the magnetic field in the solenoid to explore the full cycle of the hysteresis loop.

The L-154 is a fast and reliable analog and digital input and output device for IBM-compatible personal computers. The L-154 board is designed to convert analog signals to digital forms for a personal computer, as well as to input/output digital TTL (transistor–transistor logic) lines and control one analog output channel (digital-to-analog converter).

The magnetic field was created using a solenoid powered by a pulsed electric current. The latter can be performed in various ways, among which the most popular is the method of charging a capacitor bank to a solenoid. To obtain a pulsed magnetic field, the discharge of a battery of capacitors with a capacity of 22,500 microfarads was produced. The maximum voltage was 1000 V, and the stored energy was 11.5 kJ. The samples for measurement were placed in a special cylindrical fluoroplast mold. The mold was designed for measuring nano- and micro-sized powder materials, with mold diameter d_m = 4.40 mm and length l = 10 mm. The container with the sample was placed inside the solenoid in a system of three coils located in the region of a uniform magnetic field. Measuring coil No. 2 had 600 turns, while coils No. 1 and No. 3 each had 300 turns. Compensation coils No. 1 and No. 3, with the same flux linkage, were made of copper wire with a diameter of 0.2 mm. In the absence of a magnetic sample, a zero signal level was fixed at the output. The placement of the test sample in the measuring coil led to a violation of the sensor compensation, and the EMF induced by the sample was proportional to the time derivative of the magnetization M of the sample:

$$U(t) = \left(\frac{dM}{dH}\right)\frac{dH}{dt} = \chi\frac{dH}{dt} \quad (5)$$

where $\chi = dM/dH$—differential magnetic susceptibility. Integrating the voltage from the sensor, we calculated a voltage proportional to the magnetic moment of the sample (or, more specifically, the projection of the moment on the axis of the sensor).

A signal proportional to the magnitude of the magnetizing field was taken from a single-layer coil with a small number of turns (No. 4 = 4), and after its conversion and amplification using the AD converter it was reproduced directly on the computer display screen.

The main advantage of this method is that the measuring coils are located in such a way that the fields created by some coils of the system do not affect one another. The block diagram of the pulse magnetometer is shown in Figure 2.

The pulsed magnetic field was calibrated using a portable Universal TPU milliteslameter (ZAO «NPCentr», Nizhny Novgorod, Russia) and an inductive magnetic sensor [38]. The magnetometer was calibrated in terms of the magnetic moment by repeated measurements of standard Ni samples with a purity of at least 99.9%, and the obtained results were compared with reliable literature data [39]. An analysis of the measurement errors showed that the total statistical error in measuring the magnetization was 3%, while the error in determining the magnitude of the magnetizing field was no more than 2%.

To control the compensation in the coil system, before each measurement, the capacitors were discharged on the solenoid with the coil system without a sample. In parallel, a signal was taken from a single-layer coil with a small number of turns (No. 4 = 4), proportional to the magnitude of the magnetizing field. The signals were displayed on a personal computer monitor.

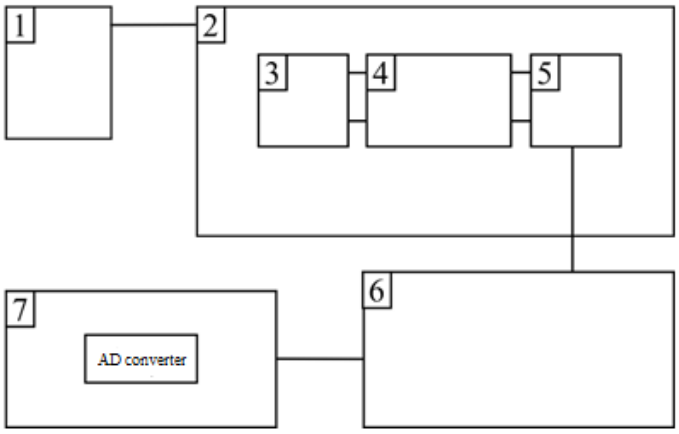

Figure 2. Block diagram of a pulse magnetometer for studying magnetic characteristics in pulsed magnetic fields: 1—an electric current pulse generation unit; 2—an impulse solenoid; 3, 5—compensation coils; 4—measuring coil; 6—a signal conversion and amplification unit; 7—AD converter.

Figure 3 shows an electrical diagram of an installation with capacitive storage. The energy stored in the capacitor bank was converted during discharge through the solenoid into the energy of the magnetic field:

$$\frac{1}{2}CU_0^2 = \frac{1}{2}\int \mu_0 H^2 dv + E_d. \quad (6)$$

where C is the battery capacity, U_0 is the initial voltage across the capacitors, H is the magnetic field strength at the time when the voltage on the batteries goes to zero, E_d is the energy spent on heating the solenoid and the conductive wires, and the integration is carried out over the entire space. In the event that the attenuation in the circuit is small, i.e., $R \ll \sqrt{(L/C)}$ (where R and L are the resistance and inductance of the circuit, respectively), the discharge has an oscillating character; this was the case in our experiment.

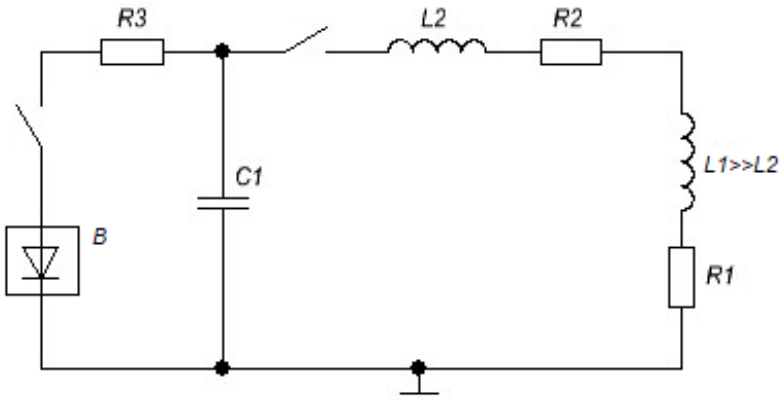

Figure 3. Electrical diagram of the installation with capacitive storage for obtaining strong magnetic fields. L1 and R1 are the inductance and resistance of the solenoid; L2 and R2 are the inductance and resistance of the lead wires; C1 is the capacity of the capacitor bank; R3 is the charging resistance; B is the high-voltage rectifier.

The time dependence of the current flowing through the solenoid is described by the following expression:

$$I = \frac{U_0}{\omega L} exp\left(-\frac{R}{2L}t\right) \sin(\omega t), \quad (7)$$

where $\omega = \omega_0\sqrt{1+\gamma^2}$; $\omega_0 = 1/LC$; $\gamma = (1/2)R\sqrt{C/L}$.

At the moment of the first maximum, the current I is [31]

$$I_{max} = \frac{U_0}{\sqrt{L/C}} exp\left(-\frac{R}{2L\omega} arctg\frac{2L\omega}{R}\right). \quad (8)$$

where $L = L1 + L2$; $R = R1 + R2$; $L1$, $R1$ and $L2$, $R2$ are the inductances and resistances of the solenoid and lead wires, respectively. To effectively convert the stored energy into the energy of the magnetic field, it is necessary to reduce the losses in the supply wires, i.e., to create structures in which $L2$ and $R2$ are small compared to $L1$ and $R1$. The condition of small losses in the pulsed magnet itself can be written as follows:

$$R1/2L1 \ll 1/\sqrt{LC} \quad (9)$$

The field amplitude can be related to the maximum current through the solenoid [37]:

$$B_m = (\mu_0 N I_{max}/r_1)\varphi(\alpha, \beta) \quad (10)$$

where N is the number of turns in the solenoid, r_1 is the inner radius of the solenoid, $\alpha = r_1/r_2$, $\beta = b/r_1$, and r_2 and b are the outer radius and half the length of the solenoid, respectively. The function $\varphi(\alpha,\beta)$ describes the dependence of the field on the shape of the solenoid, and its specific form is characterized by the type of winding [40].

In the most general case, to find the current in the simplest LRC circuit (Figure 3), which corresponds to the installation scheme with capacitive storage, it is necessary to solve a system of two differential equations:

$$L\frac{d^2I}{dt^2} + 2\frac{dI}{dt}\frac{dL}{dt} + I\frac{d^2I}{dt^2} + [R_0 + R(T)]\frac{dI}{dt} + \frac{1}{C}I = 0; \quad (11)$$

$$\frac{dT}{dt} = \frac{I^2(t)R(T)}{D_0 \nu c(T)}, \quad (12)$$

where R_0 and $R(T)$ are the temperature-independent and temperature-dependent parts of the circuit resistance, respectively, T is the conductor temperature, and D_0, ν, and $c(T)$ are the density, volume, and specific heat capacity of the conductor, respectively. It is also important to note that solenoids designed to repeatedly generate pulsed fields usually change their geometry slightly during the pulse, so the change in their inductance from specific heat can be neglected. The same can be applied to the dependence of the specific heat on the geometry of the solenoid and its changes during the pulse.

2.3. Structural and Morphological Properties of the Samples

X-ray diffraction and X-ray diffraction studies were carried out on an XRD-6000 polycrystalline diffractometer (SHIMADZU, Kyoto, Japan) with the implementation of the X-ray diffraction geometry in the Bragg–Brentano geometry with a focusing pyrographite crystal monochromator on a secondary beam of gamma rays. The radiation used was Cu-K_α (λ = 1.5406 Å). For a qualitative analysis of the phase composition, the PDF4+ X-ray powder diffraction computer database of the International Center for Diffraction Data (ICDD, Denver, CO, USA) was used. Quantitative analysis of the phase composition and refinement of the structural parameters of the detected phases were performed using the full-profile analysis program Powder Cell 2.4. Based on the analysis of the half-width and shape of the diffraction peaks using the Williamson–Hall formula, the sizes of the coherent scattering regions (CSRs) (d) and the values of the crystal lattice's relative microdistortions (ε) were calculated as follows:

$$\beta = \frac{\lambda}{dcos\theta} + 4\varepsilon tg\theta, \quad (13)$$

where β is the reflex width at half height, λ is the X-ray wavelength, and θ is the peak angular position.

To determine the fields of magnetocrystalline anisotropy along the hexagonal axis, we studied the ferromagnetic resonance spectra of $BaFe_{12}O_{19}$ oxide ferrimagnet powders. The FMR spectra were measured according to the standard waveguide "passing through" technique in the frequency range 37–53 GHz, using an automated radio spectroscope. The measurements were carried out at room temperature. To study the FMR, powder samples were placed in thin-walled quartz tubes with an inner diameter of 0.8 mm and a length of 12 mm. The density of the powder samples was approximately the same and amounted to ≈2.5 g/cm^3. The tubes were placed in a rectangular waveguide parallel to the wide wall of the waveguide so that the alternating magnetic field was oriented along the sample axis. The constant magnetizing field was directed perpendicular to the wide wall of the waveguide. The method for processing the experimental FMR data to determine the fields of magnetocrystalline anisotropy is described in detail in [41–43].

To study the structure of the materials considered in this work, a VEGA 3 SBH scanning electron microscope (SEM) (TESCAN, Brno, Czech Republic) and an ANALYSETTE 22 NanoTec laser particle size analyzer (Fritsch, Idar-Oberstein, Germany) were used. Each sample was introduced into a closed circuit with circulating liquid. The built-in ultrasonic emitter caused the destruction of particle agglomerates to obtain an accurate distribution of particles.

3. Results and Discussion

Figure 4 shows the X-ray patterns of the hexagonal ferrimagnets studied in this work, fabricated by various synthesis methods. The results of the XRD studies are presented in Table 1.

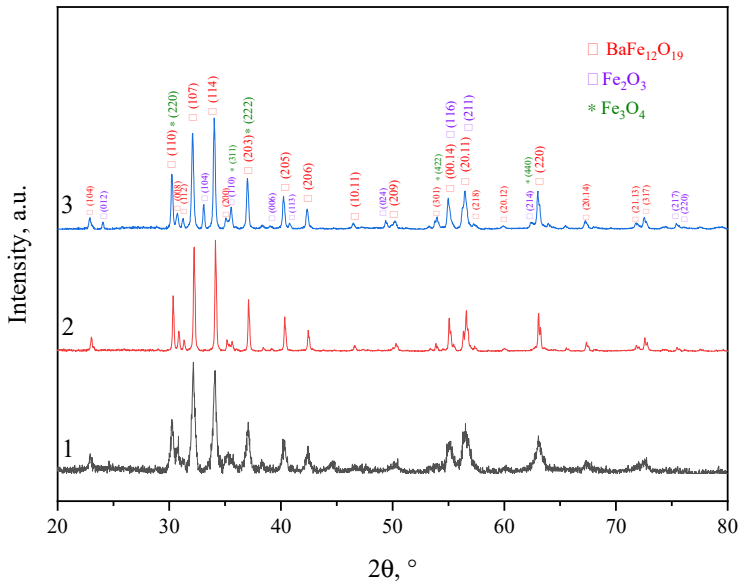

Figure 4. X-ray diffraction diagrams: sample N1 (black), sample N2 (red), sample N3 (blue). The numbers 1,2,3 correspond to the names of the samples.

Table 1. Structural and phase properties of the samples.

Sample, N	M-Phase, %	Fe_3O_4, %	α-Fe_2O_3, %	lattice Constant, Å		CSR, nm	$\varepsilon \times 10^4$	D [a]
				a	*c*			
1	97.7	2.3	0.0	5.8806	23.1388	72	-1.8 ± 0.6	35 ± 15 µm
2	100	0.0	0.0	5.8940	23.3130	60	-3.3 ± 0.7	510 ± 100 nm
3	92.2	0.0	7.8	5.9170	23.3302	67	-1.4 ± 0.7	220 ± 50 nm

[a] D—data obtained from analysis of particle size distribution (ANALYSETTE 22 NanoTec).

Analysis of Table 1 proves that an almost-pure phase of barium hexaferrite $BaFe_{12}O_{19}$ (M-phase) may be obtained by means of all of the applied synthesis methods. In sample N1 (standard ceramic technology), there was an insignificant content of magnetite (Fe_3O_4), at 2.3%. In sample N3 (sol–gel technology), there was a high content of the M-phase (92.2%), with an impurity of 7.8% hematite (α-Fe_2O_3). The formation of the main phase when using this method occurred at low temperatures, in contrast to mechanochemical synthesis and ceramic technology.

The application of the mechanochemical method (sample N2) led to an M-phase content of 100% in the material. The formation of pure M-type ferrite occurred due to the use of hydrated reagents in the synthesis after mechanochemical activation and calcination at 1100 °C. The formation of nuclei during mechanochemical synthesis with the use of hydrated compounds is much easier. Furthermore, the use of hydrated reagents accelerates diffusion transport, resulting in a rapid growth of the solid phase. Excess water released during the neutralization reaction increases the rate of formation of the M-phase compared to conventional solid-phase synthesis and creates conditions for the hydrothermal process, in which it acts as a solvent [33].

The calculated coherent scattering regions for all samples are presented in Table 1. Despite the fact that the CSR values for all synthesis technologies were approximately equal, the particle sizes differed significantly from one another. This was due to the formation of agglomerates from crystallites. Since the largest number of agglomerated particles was observed using ceramic technology, various modes of mechanical activation (MA) were added to obtain a nanosized powder. However, powder grinding by this method leads to an unacceptable significant change in the phase composition, as described in [44]. Moreover, MA, even in the "soft mode", leads to the appearance of an amorphous phase. Both of these factors affect the magnetic properties and quality of the material. When using mechanochemical and sol–gel methods for the synthesis of ferrites, nanosized particles of regular hexagonal shape (Figure 5) are produced without additional processing of the synthesized product. This fact makes the listed methods the most favorable for the synthesis of magnetic nanoparticles. The average particle sizes (D) of all three samples are presented in Table 1.

The hysteresis loops taken with the developed pulsed magnetometer are shown in Figure 6. The magnetic characteristics were measured in pulsed magnetic fields of up to 26 kOe. All samples demonstrated a wide hysteresis loop, which is typical of hard magnetic materials such as $BaFe_{12}O_{19}$ hexaferrite. The main magnetic characteristics, including the defined magnetocrystalline anisotropy fields, are presented in Table 2.

Table 2. Magnetic characteristics of samples (the measurements were carried out at 300 K).

Sample, N	M_s [a], emu/g	M_r [b] emu/g	H_c [c], kOe	M_r/M_s [d], Rel. Units	H_a [e], kOe
1	72.1 ± 2.2	32.2 ± 1.6	1.9 ± 0.1	0.4	16.7 ± 0.1
2	78.6 ± 2.4	39.3 ± 1.9	4.5 ± 0.2	0.5	15.4 ± 0.1
3	66.7 ± 2.0	34.1 ± 1.7	6.7 ± 0.3	0.5	15.4 ± 0.1

[a] M_s—saturation magnetization; [b] M_r—remanent magnetization; [c] H_c—coercivity; [d] M_r/M_s—squareness factor; [e] H_a—anisotropy field (calculated from FMR curve analysis).

The saturation magnetization M_s of sample N2 was 78.6 ± 2.4 emu/g. This value is higher than the M_s for a polycrystalline sample, which is 72 emu/g [1]. This is due to the occurrence of a paraprocess because of the presence of low-dimensional particles in the material, as well as to surface defects (i.e., breaking of bonds between the interaction of cations through oxygen ions in the octahedral sublattice). Both factors can lead to an increase in the value of saturation magnetization [45]. The M_s value of sample N1 practically corresponded to the data from the literature. According to [46], for ground polycrystal, the value of M_s should decrease. In our case, this was not observed, due to the presence of 2.3% of the magnetite phase in the sample, which had a high saturation magnetization value of 92–100 emu/g [1]. The saturation magnetization of sample N3

was 66.7 ± 2.0 emu/g. This value is slightly lower than that of a polycrystal, despite the occurrence of a paraprocess under high magnetic fields, since the sample contains a weak ferrimagnetic phase α-Fe_2O_3.

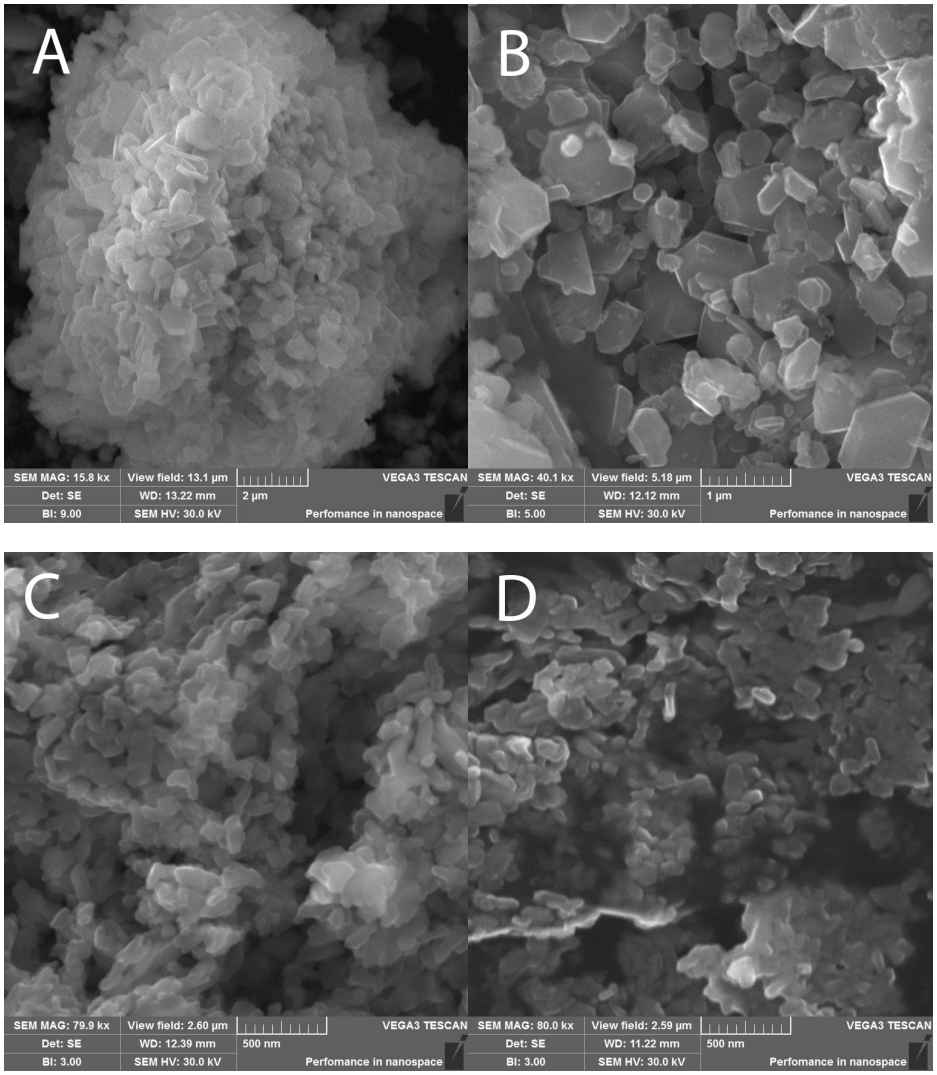

Figure 5. SEM images of final products: (**A**,**B**)—sample N2; (**C**,**D**)—sample N3.

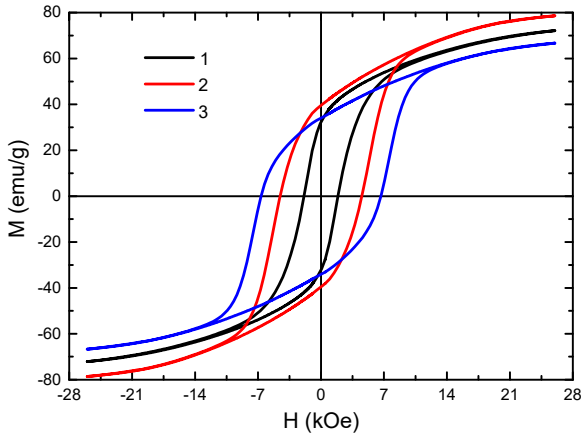

Figure 6. Hysteresis loops of $BaFe_{12}O_{19}$ synthesized by various methods: 1—ceramic method, 2—mechanochemical method, 3—sol–gel method. The measurements were carried out at 300 K.

The highest value of the coercive force was observed for sample N3, obtained by the sol–gel technology. This was associated with the particle size close to the single-domain state (Figure 5). The single-domain state of the particles of this material was confirmed as having the M_r/M_s ratio presented in Table 2. For sample N3, it was close to 0.5. According to [47], this value is typical for the processes of magnetization of randomly oriented single-domain particles of uniaxial magnets with magnetic ordering of the easy axis (EA) type, including $BaFe_{12}O_{19}$ hexaferrites. Sample N1 had the lowest H_c value of the samples tested, owing to the large particle size in the sample [48]. As a result of the grinding of a polycrystalline material to a micro-sized state, the fraction of the surface energy of the domain boundaries increases and becomes comparable to the total volume energy. Consequently, the single-domain state of particles in such materials is considered to be more energetically favorable. This leads to an increase in the magnetization reversal field of the particle and, as a result, in the value of the coercive force as well. Since the coercive force has a complex dependence on the particle size, it can be concluded that the particles of the sample synthesized by the standard ceramic technology are far from the single-domain state (290 nm) [48]. In this regard, the coercive force of this sample has low values.

4. Conclusions

A pulsed magnetometer was developed that can be used to measure the full cycle of hysteresis loops of magnetic materials in pulsed magnetic fields. The pulse magnet used in the developed installation can create magnetic fields of up to 100 kOe, making it possible to study a wide range of bulk and powder magnetic materials.

Synthesis of $BaFe_{12}O_{19}$ oxide hexagonal ferrimagnets was carried out using standard ceramic technology, sol–gel technology, and mechanochemical methods. Using various methods for the synthesis of hexaferrite, we studied the changes in the phase composition, structure, and magnetic properties of the finished products. The results of X-ray phase analysis showed that it is possible to obtain $BaFe_{12}O_{19}$ hexaferrite with a 100% M-phase content by using the mechanochemical method, due to the use of hydrated reagents in the synthesis, which accelerate the growth of crystallite nuclei in the main phase. The sol–gel technology and the ceramic method led to the appearance of impurity phases of hematite (7.8%) and magnetite (2.3%), respectively. Using the sol–gel technology, the preparation of $BaFe_{12}O_{19}$ may be carried out at a significantly lower synthesis temperature (850 °C) to obtain the main M-phase.

The study of the particle size distribution of the samples showed that particles of a regular hexagonal shape and an average size of 510 nm were produced via the mechanochemical method. The use of sol–gel technology led to the synthesis of ferrite with a low particle size (220 nm).

Analysis of the hysteresis loops measured by the developed pulse magnetometer proved the influence of the chosen synthesis method on the magnetic properties of the obtained M-type ferrites, in terms of both the saturation magnetization and the coercive force. Thus, it can be concluded that the use of different technologies can make it possible to produce a material of the same composition for various practical applications.

Author Contributions: Conceptualization, D.V.W. and K.V.K.; methodology, V.A.Z.; software, K.V.K.; investigation, D.V.W., K.V.K., V.A.Z. and R.V.M.; writing—original draft preparation, D.V.W. and O.A.D.; writing—review and editing, D.V.W. and O.A.D.; visualization, K.V.K. and V.A.Z.; project administration, D.V.W.; funding acquisition, D.V.W. All authors have read and agreed to the published version of the manuscript.

Funding: This research was funded by Russian Science Foundation, grant number 22-79-00074, https://rscf.ru/en/project/22-79-00074/ (accessed on 12 December 2022).

Data Availability Statement: The authors declare that the data supporting the findings of this study are available within the article.

Acknowledgments: The authors are grateful to Natalia Sergeevna Trufanova (Tomsk State University of Control Systems and Radioelectronics) for her help in studying the particle size distributions of the ferrites synthesized in this work.

Conflicts of Interest: The authors declare no conflict of interest.

References

1. Smit, J.; Wijn, H.P.J. *Ferrites, Physical Properties of Ferrimagnetic Oxides in Relation to Their Technical Applications*; Philips Technical Library: Eindhoven, The Netherlands, 1959; pp. 232–272.
2. Pullar, R.C. Hexagonal ferrites: A review of the synthesis, properties and applications of hexaferrite ceramics. *Prog. Mater. Sci.* **2012**, *57*, 1191–1334. [CrossRef]
3. Jotania, R.B.; Virk, H.S. Y-type Hexaferrites: Structural, Dielectric and Magnetic Properties. *Solid State Phenom.* **2012**, *189*, 209–232. [CrossRef]
4. Granados-Miralles, C.; Jenuš, P. On the potential of hard ferrite ceramics for permanent magnet technology—A review on sintering strategies. *J. Phys. D Appl. Phys.* **2021**, *54*, 303001. [CrossRef]
5. Sirisathitkul, C.; Sirisathitkul, Y. Recent Developments in 3D Printing of Rare-Earth-Free Permanent Magnets. *Inventions* **2022**, *7*, 71. [CrossRef]
6. Swapnalin, J.; Koneru, B.; Banerjee, P.; Natarajan, S.; Franco, A., Jr. Multilayer intercalation: MXene/cobalt ferrite electromagnetic wave absorbing two-dimensional materials. *J. Phys. Chem. Solids.* **2022**, *168*, 110797. [CrossRef]
7. Zahid, M.; Siddique, S.; Anum, R.; Fayzan Shakir, M.; Nawab, Y.; Rehan, Z.A. M-Type Barium Hexaferrite-Based Nanocomposites for EMI Shielding Application: A Review. *J. Supercond. Novel Magn.* **2021**, *34*, 1019–1045. [CrossRef]
8. Zavislyak, I.V.; Popov, M.A. Passive Ferrite Resonator-Based Millimeter Wave Band Components. In Proceedings of the 2017 IEEE First Ukraine Conference on Electrical and Computer Engineering (UKRCON), Kyiv, Ukraine, 29 May 2017–2 June 2017; pp. 80–83.
9. Polley, K.; Alam, T.; Bera, J. Synthesis and characterization of $BaFe_{12}O_{19}$-$CoFe_2O_4$ ferrite composite for high-frequency antenna application. *J. Aust. Ceram. Soc.* **2020**, *56*, 1179–1186. [CrossRef]
10. Polley, K.; Kundu, R.; Nayak, N.; Agarwal, R.; Bera, J. Sintering and electromagnetic properties of $BaFe_{12}O_{19}$ ferrite prepared by co-precipitation method. *J. Mater. Sci. Mater. Electron.* **2022**, *33*, 17912–17922. [CrossRef]
11. Kamran, M.; Anis-ur-Rehman, M. Enhanced transport properties in Ce doped cobalt ferrites nanoparticles for resistive RAM applications. *J. Alloys Comp.* **2020**, *822*, 153583. [CrossRef]
12. Kalaiselvan, C.R.; Laha, S.S.; Somvanshi, S.B.; Tabish, T.A.; Thorat, N.D.; Kumar Sahu, N. Manganese ferrite ($MnFe_2O_4$) nanostructures for cancer theranostics. *Coord. Chem. Rev.* **2022**, *473*, 214809. [CrossRef]
13. Andrade, R.G.D.; Ferreira, D.; Veloso, S.R.S.; Santos-Pereira, C.; Castanheira, E.M.S.; Côrte-Real, M.; Rodrigues, L.R. Synthesis and Cytotoxicity Assessment of Citrate-Coated Calcium and Manganese Ferrite Nanoparticles for Magnetic Hyperthermia. *Pharmaceutics* **2022**, *14*, 2694. [CrossRef] [PubMed]
14. Darwish, M.S.A.; Kim, H.; Lee, H.; Ryu, C.; Young Lee, J.; Yoon, J. Engineering Core-Shell Structures of Magnetic Ferrite Nanoparticles for High Hyperthermia Performance. *Nanomaterials* **2020**, *10*, 991. [CrossRef] [PubMed]
15. Javed, F.; Abbas, M.A.; Asad, M.I.; Ahmed, N.; Naseer, N.; Saleem, H.; Errachid, A.; Lebaz, N.; Elaissari, A.; Ahmad, N.M. Gd^{3+} Doped $CoFe_2O_4$ Nanoparticles for Targeted Drug Delivery and Magnetic Resonance Imaging. *Magnetochemistry* **2021**, *7*, 47. [CrossRef]
16. Lo Faro, M.; Zignani, S.C.; Aricò, A.S. Lanthanum Ferrites-Based Exsolved Perovskites as Fuel-Flexible Anode for Solid Oxide Fuel Cells. *Materials* **2020**, *13*, 3231. [CrossRef] [PubMed]
17. Naiden, E.P.; Zhuravlev, V.A.; Minin, R.V.; Susliaev, V.I.; Itin, V.I.; Korovin, E.Y. Structural and Magnetic Properties of SHS-Produced Multiphase W-Type Hexaferrites: Influence of Radiation-Thermal Treatment. *Int. J. Self-Propag. High-Temp. Syn.* **2015**, *24*, 148–151. [CrossRef]
18. Minin, R.V.; Itin, V.I.; Zhuravlev, V.A. Effect of mechanical activation and ferritization on the phase composition of W-type hexaferrites obtained by the method of selfpropagating high-temperature synthesis. *J. Phys. Conf. Series.* **2020**, *1459*, 012016. [CrossRef]
19. Leal, E.; Basilio, S.T.; Dantas, J.; Richa, P.; Lima, R.D.C.; Kiminami, R.H.G.A.; Costa, A.C.F.D.M. Structural, textural, morphological, magnetic and electromagnetic study of Cu-doped NiZn ferrite synthesized by pilot-scale combustion for RAM application. *Arab. J. Chem.* **2020**, *13*, 8100–8118. [CrossRef]
20. Jotania, B.R.; Patel, P.A. Microstructure and dielectric properties of Mn substituted $Sr_2Cu_2Fe_{12}O_{22}$ (Cu_2Y) hexaferrite powder. *IJERA* **2012**, *2*, 494–498.
21. Naem Ashiq, M.; Asi, A.S.; Farooq, S.; Najam-ul-Haq, M.; Rehman, S. Magnetic and electrical properties of M-type nano-strontium hexaferrite prepared by sol-gel combustion method. *J. Magn. Magn. Mater.* **2017**, *444*, 426–431. [CrossRef]
22. Kefeni, K.K.; Msagati, T.A.M.; Mamba, B.B. Ferrite nanoparticles: Synthesis, characterisation and applications in electronic device, Mater. *Sci. Eng. B* **2017**, *215*, 37–55. [CrossRef]
23. Dairy, A.R.A.; Al-Hmoud, L.A.; Khatatbeh, H.A. Magnetic and Structural Properties of Barium Hexaferrite Nanoparticles Doped with Titanium. *Symmetry* **2019**, *11*, 732. [CrossRef]

24. Maltoni, P.; Ivanov, S.A.; Barucca, G.; Varvaro, G.; Peddis, D.; Mathieu, R. Complex correlations between microstructure and magnetic behavior in $SrFe_{12}O_{19}$ hexaferrite nanoparticles. *Sci. Rep.* **2021**, *11*, 23307. [CrossRef] [PubMed]
25. Mukhortova, Y.R.; Pryadko, A.S.; Chernozem, R.V.; Pariy, I.O.; Akoulina, E.A.; Demianova, I.V.; Zharkova, I.I.; Ivanov, Y.F.; Wagner, D.V.; Bonartsev, A.P.; et al. Fabrication and characterization of a magnetic biocomposite of magnetite nanoparticles and reduced graphene oxide for biomedical applications. *Nano-Struct. Nano-Objects* **2022**, *29*, 100843. [CrossRef]
26. Pryadko, A.S.; Botvin, V.V.; Mukhortova, Y.R.; Pariy, I.; Wagner, D.V.; Laktionov, P.P.; Chernonosova, V.S.; Chelobanov, B.P.; Chernozem, R.V.; Surmeneva, M.A.; et al. Core-Shell Magnetoactive PHB/Gelatin/Magnetite Composite Electrospun Scaffolds for Biomedical Applications. *Polymers* **2022**, *14*, 529. [CrossRef]
27. Kovacs, G.; Kuczmann, M. Measuring and the hysteresis characteristics of permanent magnet. *Phys. B Condens. Matter* **2018**, *549*, 62–68. [CrossRef]
28. Gersdorf, R.; Muller, F.A.; Roeland, L.W. Design of High Field Magnet Coils for Long Pulses. *Rev. Sci. Instrum.* **1965**, *36*, 1100–1109. [CrossRef]
29. Kapitsa, P.L. A method of producing strong magnetic fields. *Proc. R. Soc. London. Ser. A Contain. Pap. A Math. Phys. Character* **1924**, *105*, 691.
30. Freudenberger, J.; Lyubimova, J.; Gaganov, A.; Witte, H.; Hickman, A.L.; Jones, H.; Nganbe, M. Non-destructive pulsed field CuAg-solenoids. *Mater. Sci. Eng. A.* **2010**, *527*, 2004–2013. [CrossRef]
31. Lecouturier, F.; Billette, J.; Béard, J.; Debray, F.; Ferreira, N.; Tudela, J.M.; Rikken, G.; Frings, P. Copper/Stainless Steel Polyhelix Magnets. *IEEE Trans. Appl. Supercond.* **2012**, *22*, 4300404. [CrossRef]
32. Bitter, F. The Design of Powerful Electromagnets Part IV. The New Magnet Laboratory at M. I. T. *Rev. Sci. Instrum.* **1939**, *10*, 373–381.
33. Zhuravlev, V.A.; Nevmyvaka, A.A.; Itin, V.I.; Svetlichnyi, V.A.; Lapin, I.N.; Wagner, D.V. Influence of the reagent types on the characteristics of barium hexaferrites prepared by mechanochemical method. *Mater. Today Commun.* **2019**, *21*, 100614. [CrossRef]
34. Bahadur, D.; Rajakumar, S.; Kumar, A. Influence of fuel ratios on auto combustion synthesis of barium ferrite nano particles. *J. Chem. Sci.* **2006**, *118*, 15–21. [CrossRef]
35. Huang, J.; Zhuang, H.; Li, W. Synthesis and characterization of nano crystalline $BaFe_{12}O_{19}$ powders by low temperature combustion. *Mater. Res. Bull.* **2003**, *38*, 149–159. [CrossRef]
36. Affleck, L.; Auguas, M.D.; Parkin, I.P.; Pankhurst, Q.A.; Kuznetsov, M.V. Microstructural aspects of the self-propagating high temperature synthesis of hexagonal barium ferrites in an external magnetic field. *J. Mater. Chem.* **2000**, *10*, 1925–1932. [CrossRef]
37. Montgomery, D.B. *Solenoid Magnet Design: The Magnetic and Mechanical Aspects of Resistive and Superconducting Systems*; Wiley-Interscience: New York, NY, USA, 1969; p. 312.
38. Knoepfel, H. *Pulsed High Magnetic Fields: Physical Effects and Generation Methods Concerning Pulsed Fields up to the Megaoersted Level*; North Holland: Amsterdam, The Netherlands, 1970; p. 372.
39. Wohlfarth, E.P. *Handbook of Magnetic Materials*; North Holland: Amsterdam, The Netherlands, 1980; p. 603.
40. Strakhovskii, G.M.; Kravtsov, N.V. Strong magnetic fields. *Sov. Phys. Usp.* **1960**, *3*, 260–272. [CrossRef]
41. Zhuravlev, V.A. Ferromagnetic resonance in the polycrystalline hexagonal ferrites $Co_{2-x}Zn_xW$. *Physics of the Solid State.* **1999**, *41*, 956–959. [CrossRef]
42. Zhuravlev, V.A.; Meshcheryakov, V.A. Magnetic Susceptibility Tensor of Anisotropic Ferromagnetic Magnetized Media. *Russ. Phys. J.* **2014**, *56*, 1387–1397. [CrossRef]
43. Zhuravlev, V.A.; Naiden, E.P. Ferromagnetic resonance in hexaferrite nanopowders. *Russ. Phys. J.* **2008**, *51*, 38–44. [CrossRef]
44. Zhuravlev, V.A.; Naiden, E.P. Influence of the mechanical activation modes on the structure parameters and magnetic properties of Z-type hexaferrite $Ba_3Co_{2.4}Ti_{0.4}Fe_{23.2}O_{41}$ nanopowders. *Russ. Phys. J.* **2008**, *51*, 902–906. [CrossRef]
45. Pryadko, A.S.; Mukhortova, Y.R.; Chernozem, R.V.; Shlapakova, L.E.; Wagner, D.V.; Romanyuk, K.; Gerasimov, E.Y.; Kholkin, A.; Surmenev, R.A.; Surmeneva, M.A. Comprehensive Study on the Reinforcement of Electrospun PHB Scaffolds with Composite Magnetic Fe_3O_{4-r}GO Fillers: Structure, Physico-Mechanical Properties, and Piezoelectric Response. *ACS Omega.* **2022**, *7*, 41392–41411. [CrossRef]
46. Batlle, X.; Labarta, A. Finite-size effects in fine particles: Magnetic and transport properties. *J. Phys. D Appl. Phys.* **2002**, *35*, R15–R42.
47. Stoner, E.C.; Wohlfart, E.P. A Mechanism of Magnetic Hysteresis in Heterogeneous Alloys. *IEEE Trans. Magn.* **1991**, *27*, 3475–3518. [CrossRef]
48. Skomski, R. Nanomagnetics. *J. Phys. Cond. Matter* **2003**, *15*, R841. [CrossRef]